Journal of Electron Spectroscopy and Related Phenomena 166–167 (2008) 3–10

Contents lists available at ScienceDirect

Journal of Electron Spectroscopy and Related Phenomena

journal homepage: www.elsevier.com/locate/elspec

Interatomic Coulombic decay following the Auger decay: Experimental evidence in rare-gas dimers

K. Ueda[a,*], H. Fukuzawa[a], X.-J. Liu[a], K. Sakai[a], G. Prümper[a], Y. Morishita[b], N. Saito[b], I.H. Suzuki[b,c], K. Nagaya[d], H. Iwayama[d], M. Yao[d], K. Kreidi[e], M. Schöffler[f], T. Jahnke[f], S. Schössler[f], R. Dörner[f], Th. Weber[g], J. Harries[h], Y. Tamenori[h]

[a] *Institute of Multidisciplinary Research for Advanced Materials, Tohoku University, Sendai 980-8577, Japan*
[b] *National Institute of Advanced Industrial Science and Technology (AIST), NMIJ, Tsukuba 305-8568, Japan*
[c] *Photon Factory, Institute of Materials Structure Science, Tsukuba 305-0801, Japan*
[d] *Department of Physics, Kyoto University, Kyoto 606-8502, Japan*
[e] *DESY, Notkestrasse 85, Hamburg 22607, Germany*
[f] *Goethe-Universität Frankfurt am Main, Max-von-Laue-Str. 1, Frankfurt D-60438, Germany*
[g] *Lawrence Berkeley National Laboratory, Berkeley, CA 94720, USA*
[h] *Japan Synchrotron Radiation Research Institute, Sayo, Hyogo 679-5198, Japan*

ARTICLE INFO

Article history:
Available online 25 March 2008

Keywords:
Interatomic Coulombic decay
Rare-gas dimer
Auger decay
Coincidence

ABSTRACT

Interatomic Coulombic decay (ICD) in Ar_2, ArKr and Kr_2 following Ar 2p or Kr 3d Auger decay has been investigated by means of momentum-resolved electron–ion–ion coincidence spectroscopy. This sequential decay leads to Coulombic dissociation into dication and monocation. Simultaneously determining the kinetic energy of the ICD electron and the kinetic energy release between the two atomic ions, we have been able to unambiguously identify the ICD channels. We find that, in general, spin-conserved ICD, in which the singlet (triplet) dicationic state produced via the atomic Auger decay preferentially decays to the singlet (triplet) state, transferring the energy to the other atom, is faster than spin-flip ICD, in which the Auger final singlet (triplet) dicationic state decays to the triplet (singlet) state. However, spin-flip ICD may take place when spin-conserved ICD becomes energetically forbidden. Dipole-forbidden ICDs from $Kr^{2+}(4s^{-2}\,{}^1S)$–B (B = Ar or Kr) to $Kr^{2+}(4p^{-2}\,{}^1D,\ {}^3P)$–$B^+$ are also observed.

1. Introduction

Inner-shell ionization of atoms and molecules leads to the formation of ions with energies well above the double ionization threshold. The inner-shell ionized states can decay by the electron emission. This process is known as Auger decay [1]. Auger spectra are generally considered as fingerprint images of the atom where the inner-shell hole is created (see, for example, [2] and references therein). About a decade ago however, Cederbaum et al. [3] proposed a new mechanism of electronic decay where the environment plays a role. For isolated atoms or molecules with an *innervalence* vacancy, Auger decay is often energetically forbidden, but interatomic or intermolecular Coulombic decay (ICD) may occur when another species is in close proximity. The first experimental observation of ICD was reported by Marburger et al. [4]: they observed the ICD process in 2s ionized Ne clusters. Following this pioneering work, Jahnke et al. [5] reported clear experimental evidence for ICD in 2s ionized Ne dimers by identifying the process unambiguously using cold-target recoil ion momentum spectroscopy (COLTRIMS) [6,7].

In ICD, an atom with an innervalence vacancy transfers its energy to a neighboring species which subsequently releases its energy by emitting an electron from its outervalence orbital [3,8]. This energy transfer process can be viewed as virtual photon exchange and thus, in principle, ICD can take place without having a significant overlap of the orbitals. Using Ne_2 dimers as a specific sample, Jahnke et al. experimentally demonstrated that the ICD rates are much faster when the dipole-allowed virtual photon exchange channel is open than the dipole-forbidden ICD at the equilibrium internuclear distance [9]. Averbukh et al., on the other hand, theoretically showed that, even in loosely bound van der Waals clusters, the orbital overlap can be a crucial factor [10]. The ICD can be very fast depending on the environment [11]. For van der Waals clusters, ICD becomes faster for larger sizes [12], as confirmed by experiment [13]. Also, in analogy to resonant Auger decay [14], one can observe resonant ICD [15–17].

* Corresponding author.
E-mail address: ueda@tagen.tohoku.ac.jp (K. Ueda).

0368-2048/$ – see front matter © 2008 Elsevier B.V. All rights reserved.
doi:10.1016/j.elspec.2008.03.002

ICD can take place also after Auger decay, as a second step decay [18]. Morishita et al. [19] were the first to observe ICD after Auger decay: unambiguously identifying ICD in Ar_2 after Ar 2p Auger decay, using momentum-resolved electron–ion–ion coincidence spectroscopy (equivalent to COLTRIMS). The processes observed by Morishita et al. were further investigated theoretically by Stoychev et al. [20].

We have extended the observation of ICD after Auger decay to the rare-gas dimers ArKr and Kr_2. A report on ICD in ArKr after Ar 2p Auger decay can be found elsewhere [21]. In the present paper, we aim to compare systematically the results for three different systems Ar_2, ArKr and Kr_2. The processes we probe and discuss here are

$$[A^+(\text{core}^{-1})\text{–B}]+e^-_{\text{Photo}} \rightarrow [A^{2+}\text{–B}]+e^-_{\text{Auger}} \rightarrow A^{2+}+B^+ +e^-_{\text{ICD}}. \quad (1)$$

In our experiment, we detect the ICD electron in coincidence with the A^{2+}–B^+ ion pair and extract the correlation between the kinetic energy of the ICD electron and kinetic energy release (KER) of the ion pair.

The experimental setup and procedure are described in the following section. The results are shown in Section 3 and discussed in detail in Section 4.

2. Experiment

The experiment was carried out on the c branch of the soft X-ray photochemistry beam line 27SU [22–24] at SPring-8. The operation mode of the storage ring was the so-called several single-bunches mode, i.e., 26 single − bunches + 2/29 filling mode, with a single-bunch separation of 165.2 ns.

The cluster beam is produced by expanding a mixture of argon and krypton gases at a flow rate ratio of 6:1, at a total stagnation pressure of 3.3 bar at room temperature, through a pinhole of 50 μm diameter and 0.25 mm thickness. Under these conditions, the cluster beam includes Ar and Kr monomers, Ar_2 and Kr_2 dimers, ArKr hetero-dimers, as well as larger clusters. The cluster beam is directed vertically.

The photon beam was focused to a size of less than 0.2 mm in height and 0.5 mm in width at the point of crossing with the molecular beam. The coincidence measurements described below were performed with the electric vector E of the linearly polarized light orientated vertically, at a photon energy of 262.54 eV, i.e., ∼13.9 and ∼11.8 eV above the atomic Ar $2p^{-1}{}^2P_{3/2}$ and $2p^{-1}{}^2P_{1/2}$ ionization thresholds, i.e., 248.628 and 250.776 eV, respectively [25]. The photon bandwidth was ∼30 meV.

Our momentum-resolved electron–ion–ion coincidence spectroscopy [26–32] is based on recording the electron and ion times-of-flight (TOFs) with multi-hit two-dimensional position sensitive detectors [33]. Knowledge of position and arrival time on the particle detectors, (x, y, t), allows us to extract information about the linear momentum (p_x, p_y, p_z) for each particle. The two TOF spectrometers are placed face to face. The TOF spectrometer axis is horizontal and perpendicular to both the photon beam and the molecular beam. The lengths of the acceleration region and the drift region of the electron spectrometer are 33.7 mm and 67.4 mm, respectively. For the ion spectrometer, there are two acceleration regions and no drift region. The length of the first acceleration region is 16.5 mm and that of the second one is 82.5 mm. The TOF spectrometer for the electron is equipped with a hexagonal multi-hit position-sensitive delay-line detector of effective diameter of 120 mm, while that for the ion is of effective diameter of 80 mm.

In the present experiments, the static extraction field was set to ∼1.5 V/mm. The static field of the second acceleration region for the ions was set to ∼21 V/mm. A uniform magnetic field of 6.1 G was superimposed to the spectrometer by a set of Helmholtz coils outside the vacuum chamber. Under these conditions, all the electrons up to ∼20 eV in kinetic energy and all the ions up to ∼9 eV kinetic energy, both ejected in 4π sr, were accelerated onto the MCP detectors. The TOFs of the electrons and ions were recorded with respect to the bunch marker of the synchrotron radiation source using multi-hit time-to-digital converters (TDCs, c027, Hoshin Electronics Co., Ltd.) [34]. These TDCs have a timing resolution of about 120 ps, a multi-hit capability of up to 6 events, and a time span of 40 μs. Appropriate gates selected only those electron signals synchronized with the single bunches. We recorded only events in which at least one ion and one electron were detected in coincidence.

3. Results

The left panel of Fig. 1 shows the ion–ion coincidence TOF spectrum recorded for the Ar and Kr mixed gas. The x and y coordinates correspond to the TOFs of the first and the second ions of the coincidence pair. Very strong vertical and horizontal lines correspond to false coincidences originating from the dominant monomer contributions. One can see lines corresponding to fragmentation into Ar^+–Ar^+, Ar^{2+}–Ar^+, Kr^+–Kr^+, Kr^{2+}–Kr^+, Ar^+–Kr^+, Ar^{2+}–Kr^+, and Kr^{2+}–Ar^+. Here, we are interested in the fragmentation of the type A^{2+}–B^+. The procedure to select only the events from each of these

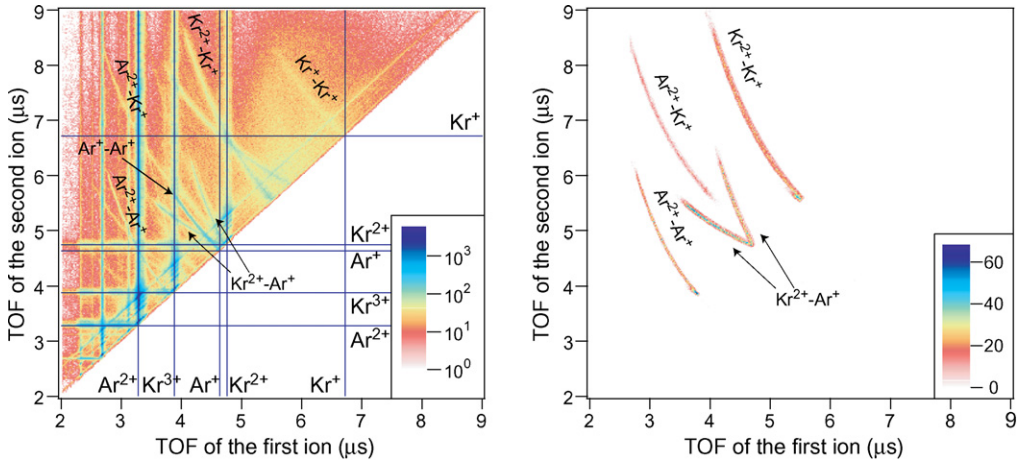

Fig. 1. Ion–ion coincidence TOF spectra: left panel, without any selections; right panel, with selections by the momentum conservation between the selected two ions whose charges are in total three and by the some of the kinetic energies of the two ions (kinetic energy release KER), $5 < \text{KER} < 10$ eV.

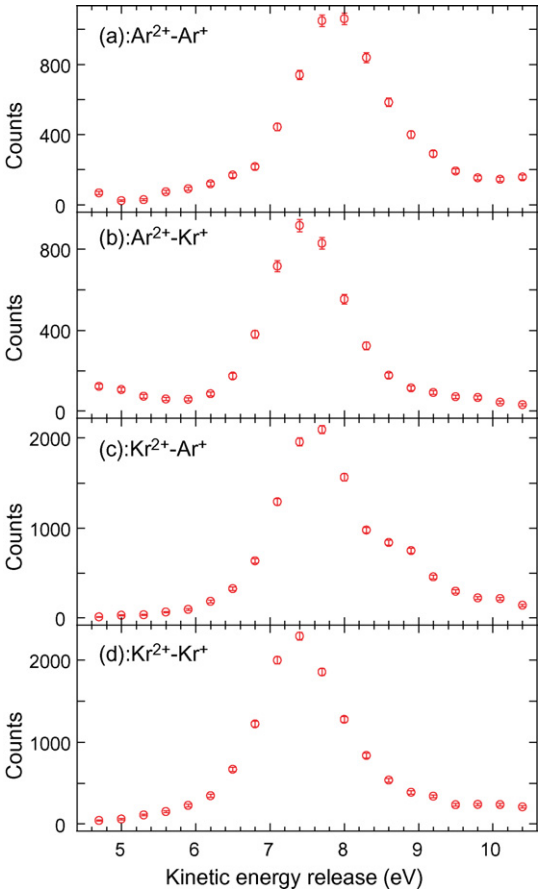

Fig. 2. The total kinetic energy release (KER) in the (a) $Ar_2{}^{3+}$ fragmentation into the Ar^{2+} and Ar^+ ions, (b) $ArKr^{3+}$ fragmentation into the Ar^{2+} and Kr^+ ions, (c) $ArKr^{3+}$ fragmentation into the Kr^{2+} and Ar^+ ions, and (d) $Kr_2{}^{3+}$ fragmentation into the Kr^{2+} and Kr^+ ions.

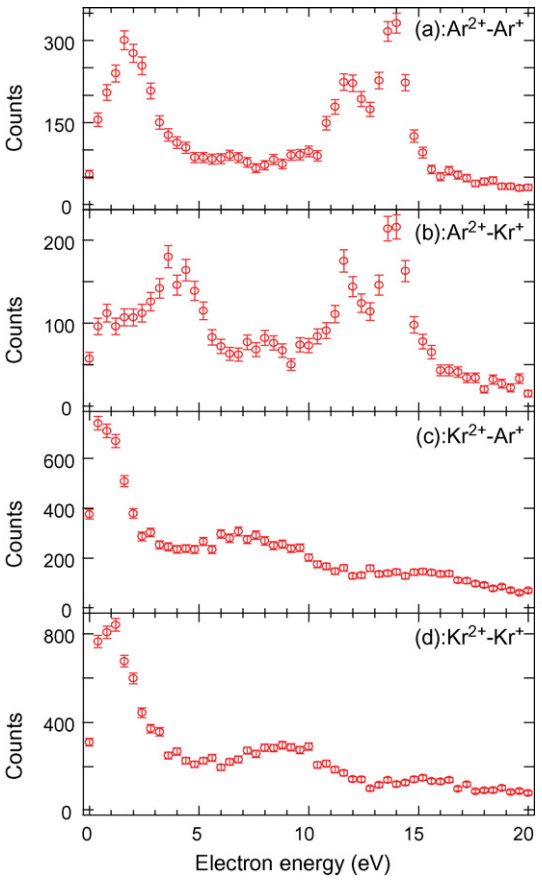

Fig. 3. Electron energy distribution of the electron ejected from (a) Ar_2 coincident with Ar^{2+} and Ar^+ ions, (b) ArKr coincident with Ar^{2+} and Kr^+ ions, (c) ArKr coincident with Kr^{2+} and Ar^+ ions, and (d) Kr_2 coincident with Kr^{2+} and Kr^+ ions.

fragmentation processes is to impose in off-line analysis an acceptance window on the vector sum of the momentum of the two ions, using the momentum conservation law. We find that the additional gate for the selection of the kinetic energy release between the two ions ($5 < KER < 10$ eV; see Fig. 2) helps suppression of the contributions from the false coincidences still remaining after the selection by the momentum sum. The results of these selections are shown in the right panel of Fig. 1. One can clearly see that these selections suppress the false coincidences almost completely. We found that changing the acceptance window of the KER range to $3 < KER < 20$ eV produces some additional small spots that are attributed to the false coincidences. We note also that the present selections of the events in the right panel of Fig. 1 in principle automatically reject ion-pair counts resulting from the explosion of larger clusters. However, these selections might not eliminate completely contamination from small clusters such as linear trimers, if the neutral fragments receive only a very small momentum. In the present measurement, the ion–ion coincidence rates relative to the total ion count rate are 0.05% for Ar^{2+}–Ar^+, 0.05% for Ar^{2+}–Kr^+, 0.1% for Kr^{2+}–Ar^+, and 0.1% for Kr^{2+}–Kr^+.

Fig. 2 shows the distribution of the KER in the fragmentation of the triply charged dimers, $(Ar_2)^{3+}$, $(ArKr)^{3+}$ and $(Kr_2)^{3+}$, into dication and monocation. The peak energies of the KER distributions (obtained by peak fitting) are 7.86, 7.61, 7.47 and 7.40 eV for $(Ar_2)^{3+} \rightarrow Ar^{2+} + Ar^+$, $(ArKr)^{3+} \rightarrow Kr^{2+} + Ar^+$, $(ArKr)^{3+} \rightarrow Ar^{2+} + Kr^+$ and $(Kr_2)^{3+} \rightarrow Kr^{2+} + Kr^+$, respectively. The fragmentation of $(ArKr)^{3+}$ into $Ar^{2+} + Kr^+$ and into $Kr^{2+} + Ar^+$ exhibit slightly different KER distributions, indicating that the electronic decay rates involved are different. If one assumes pure Coulomb explosion, these values directly reflect internuclear distances of 3.66, 3.78, 3.85 and 3.89 Å, respectively. These values are close to, or only slightly shorter than, the bond lengths of neutral Ar_2, 3.76 Å [35], ArKr, 3.88 Å [36] and Kr_2, 4.01 Å [35]. These facts suggest that both Auger decay and subsequent electronic decay, i.e., ICD, are faster than nuclear motion in the core-ionized state and Auger final dicationic states in these dimers. It is also worth noting that the widths of the KER distributions reflect approximately the spread of the ground state vibrational wavefunctions.

Fig. 3 shows the electron energy distributions coincident with Ar^{2+}–Ar^+, Ar^{2+}–Kr^+, Kr^{2+}–Ar^+ and Kr^{2+}–Kr^+. Here, the data selections are the same as those in the right panel of Fig. 1. The present coincidence spectra (Figs. 3–8) are thus practically free from the false coincidence contributions. We note that changing the KER range from $5 < KER < 10$ eV to $3 < KER < 20$ eV did not cause any significant changes in the coincidence spectra (Figs. 3–8).

Let us first focus on the spectra recorded in coincidence with Ar^{2+}–Ar^+ in Fig. 3(a) and Ar^{2+}–Kr^+ in Fig. 3(b). One can see two peaks corresponding to the Ar 2p photoelectrons that appear at kinetic energies 11.8 and 13.9 eV. In addition, a broad peak appears at ~2 eV for Ar^{2+}–Ar^+ and ~4 eV for Ar^{2+}–Kr^+. This broad structure corresponds to electron emission by ICD [19,21]. The reason why the peak energy is shifted up by ≈ 2 eV for ArKr, by changing the detected monocation from Ar^+ to Kr^+, is because the ionization energy of Kr is lower than that of Ar by ≈2 eV.

A direct proof that the ICD electrons are emitted after inner-shell ionization may be given by the 2-electron–2-ion coincidence. Fig. 4(a) and (b) depict the two dimensional electron–electron coin-

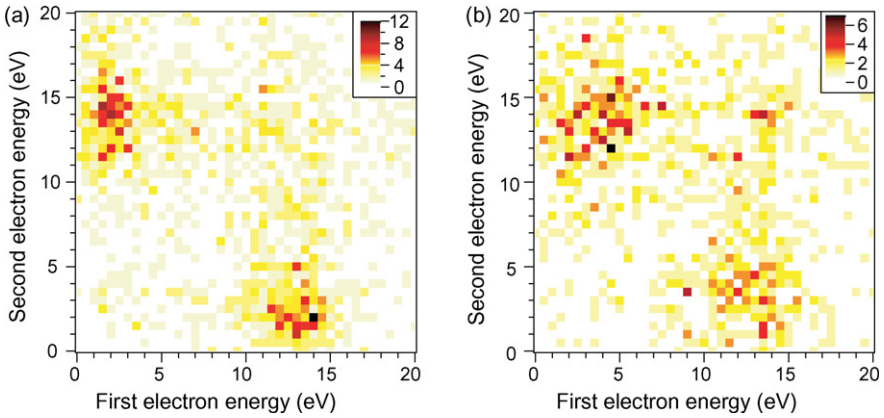

Fig. 4. Photoelectron–ICD-electron coincidence spectra for (a) Ar_2 coincident with Ar^{2+} and Ar^+ ions and (b) ArKr coincident with Ar^{2+} and Kr^+ ions.

cidence spectra recorded with Ar^{2+}–Ar^+ and Ar^{2+}–Kr^+, respectively. It is clearly seen that the ICD electrons at ∼2 eV for Ar^{2+}–Ar^+ and ∼4 eV for Ar^{2+}–Kr^+ are indeed detected in coincidence with Ar 2p photoelectrons at 11.8 and 13.9 eV that are not well resolved in the figure due to low counting rates.

Now we focus on the other two spectra in Fig. 3(c) and (d). These spectra do not exhibit Ar 2p photoelectron spectra and thus can be correlated to the electron emission after photoionization of the Kr site. In other words, the Kr^{2+}–Ar^+ pair formation following Ar 2p photoionization, which could be experimental evidence of electron-transfer-mediated decay [37], is unrecognizable. Photoelectron kinetic energies from any shells of Kr are out of the range shown in the figure. (See the next paragraph.) In the spectrum recorded in coincidence with Kr^{2+}–Kr^+(Fig. 3(d)), a broad peak at ≈1 eV, with a long high-energy tail up to ≈3.5 eV, appears. This

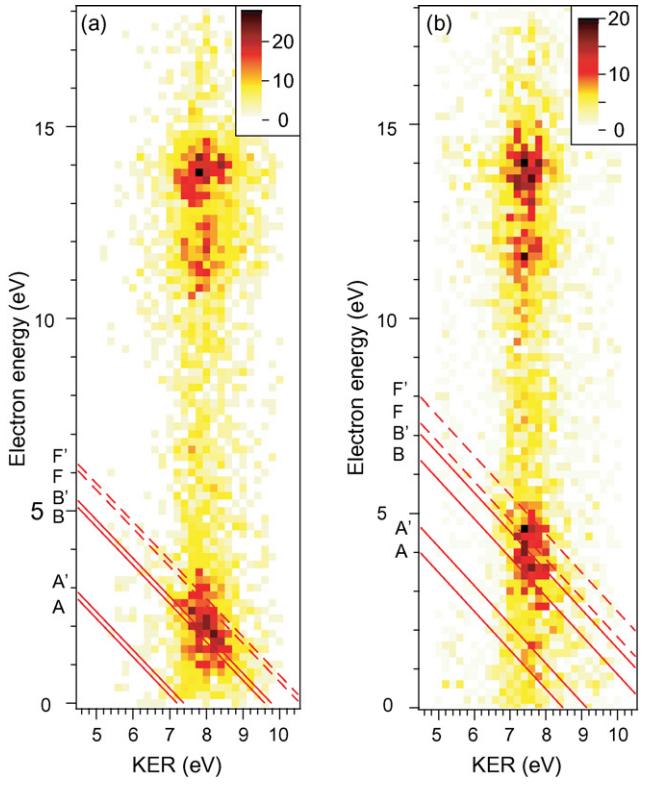

Fig. 5. Correlation between the kinetic energy of the ICD electron and the KER of (a) Ar^{2+} and Ar^+ and (b) Ar^{2+} and Kr^+. The lines with a slope of −1 correspond to spin-conserved ICD transitions.

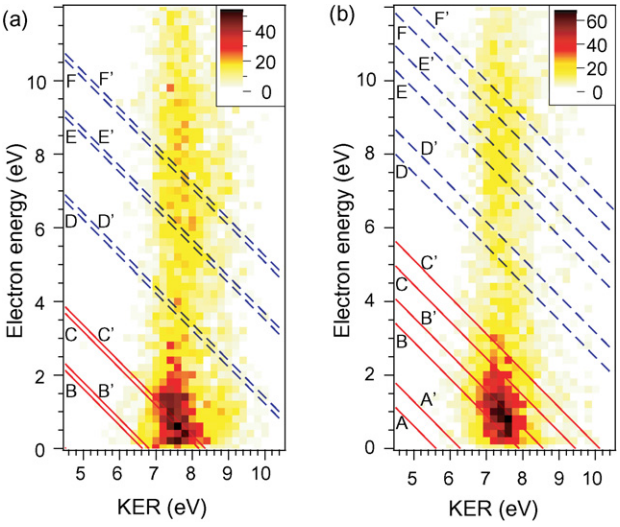

Fig. 6. Correlation between the kinetic energy of the ICD electron and the KER of (a) Kr^{2+} and Ar^+ and (b) Kr^{2+} and Kr^+. The lines with a slope of −1 correspond to the expected ICD transitions.

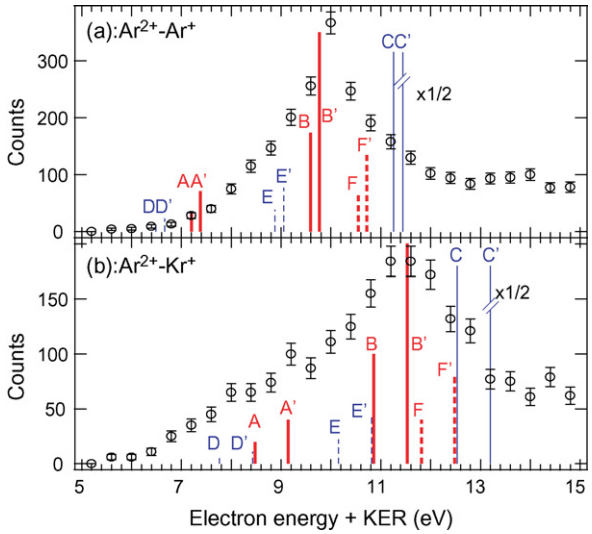

Fig. 7. The sum of the electron energy and the KER of (a) Ar^{2+} and Ar^+ and (b) Ar^{2+} and Kr^+. The solid lines correspond to the ^1P Auger final states (labels of A–C), the dotted lines the ^3P states (labels of D–F). The thick lines A, B and F (also shown in Fig. 4), correspond to spin-conserved transitions and the thin lines C, D and E correspond to spin-flip transitions.

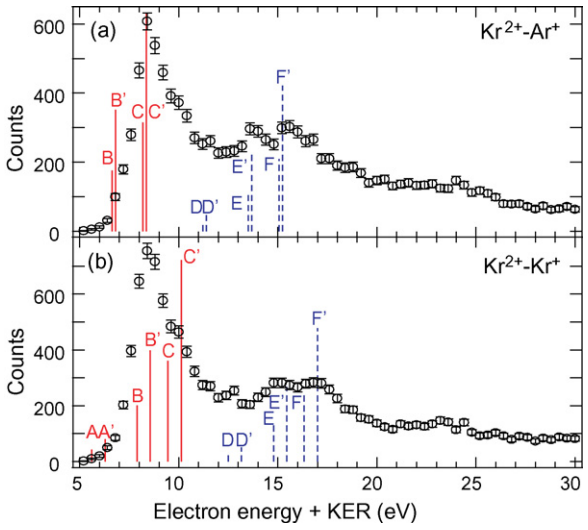

Fig. 8. The sum of the electron energy and the KER of (a) Kr^{2+} and Ar^+ and (b) Kr^{2+} and Kr^+. The solid lines correspond to the $4p^{-3}4d$ Auger final state (labels of A–C and A′–C′), the dotted lines the $4s^{-2}\,{}^1S$ state (labels of D–F and D′–F′).

structure is attributed to ICD emission. In the spectrum recorded in coincidence with Kr^{2+}–Ar^+(Fig. 3(c)), a broad peak appears at ≈1 eV. This band also corresponds to the ICD emission. At first glance, this observation is puzzling because the ionization energy of Kr is lower by ≈2 eV than Ar and thus kinetic energies of the ICD electrons in ArKr are expected to be ≈2 eV lower than those in Kr_2. We will discuss this point later. We note that there are also weak broad peaks at ≈8.5 and 7 eV coincident with Kr^{2+}–Kr^+(Fig. 3(d)) and Kr^{2+}–Ar^+(Fig. 3(c)), respectively. These are also attributed to ICD emission.

The ionization thresholds for Kr 3p are 221.8 and 214.2 eV [38] for $^2P_{3/2}$ and $^2P_{1/2}$, respectively, and those for Kr 3d are 93.788 and 95.038 eV [25] for $^2D_{5/2}$ and $^2D_{3/2}$, respectively. The ratio of the photoionization cross sections for the Kr 3p and 3d at ∼260 eV reported by Lindle et al. is 1:10 [39]. In the present setting of the electric and magnetic fields, the acceptance angles for the electrons with kinetic energy larger than 20 eV sharply drop with increasing the kinetic energy. It was just possible to detect 3p or 3d photoelectrons, but we could not extract 2-electron–2-ion coincidence spectra similar to Fig. 4.

Our coincidence measurement for one electron and two ions provides the electron kinetic energy together with the KER of the two ions for each event. The correlation between the electron energy and the KER of the two ions is shown in Fig. 5 for coincidence with Ar^{2+}–Ar^+ and Ar^{2+}–Kr^+ and in Fig. 6 for coincidence with Kr^{2+}–Ar^+ and Kr^{2+}–Kr^+. Lines with a slope of −1 correspond to the expected values for the sum of kinetic energy of the ICD electron and KER, as will be discussed in the following section.

The distributions for the energy sum of the electron kinetic energy and the KER are illustrated in Fig. 7 for coincidence with Ar^{2+}–Ar^+ and Ar^{2+}–Kr^+ and in Fig. 8 for coincidence with Kr^{2+}–Ar^+ and Kr^{2+}–Kr^+. The vertical lines correspond to the expected energy sums for the ICD transitions as will be discussed later.

The energy resolution depends on the electron and ion energies and can be estimated from the resolutions of time and position measurements by the position sensitive detector. The resolution of the electron kinetic energy varies from 0.25 eV to 1.1 eV as the kinetic energy goes from 1 eV to 14 eV. The measured full width at half maximum of the photoelectron peak at 14 eV is about 1.2 eV, in reasonable agreement with our estimate. The resolution of the ion KER is estimated to be 0.3 eV with KER at 7.5 eV. The overall energy resolution for the energy sum in Figs. 7 and 8 is the convolution of these two widths.

4. Discussion

4.1. ICDs after Ar 2p Auger decay

Let us consider first ICD in Ar_2 after Ar 2p Auger decay. Fig. 9 shows a schematic energy level diagram relevant to ICD in Ar_2 after Auger decay. In the independent particle approximation, the two-vacancy Auger final states of atomic Ar^{2+} are $3p^{-2}$, $3s^{-1}3p^{-1}$, and $3s^{-2}$. In the case of atomic Ar^{2+}, however, the independent particle approximation completely breaks down. For example, the dicationic states at 61.25 and 70.65 eV above the neutral atomic ground state are usually assigned to $3s^{-1}3p^{-1}\,{}^1P$ and $3p^{-3}3d\,{}^1P$, respectively [40,41]. In reality, however, both configurations $3s^{-1}3p^{-1}$ and $3p^{-3}3d$ are completely mixed in these states [40,41]. As a result, the Ar atomic Auger transition to the state at 70.65 eV designated as $3p^{-3}3d\,{}^1P$ occurs with significant intensity [41]. This is also the case for the states at 57.56 and 69.94 eV. Although these states are assigned to $3s^{-1}3p^{-1}\,{}^3P$ and $3p^{-3}3d\,{}^3P$, respectively, these two configurations are also severely mixed. The Auger lines to the satellite state at 69.94 eV also appear with some intensity. The intensity ratio of the Auger transitions to $3p^{-3}3d\,{}^1P$ and to $3p^{-3}3d\,{}^3P$ is roughly 3:1 [41].

The triple ionization threshold of atomic Ar (84.12 eV) is higher than all of the Auger final states discussed above, and thus these states are not subject to autoionization in an isolated Ar^{2+} dication. However, the triple ionization threshold for Ar_2 is significantly lower since the charge can be distributed to both sites. As a result, the states at 70.65 and 69.94 eV, designated as $3p^{-3}3d\,{}^1P$ and ^3P, respectively, are subject to ICD in dimers. (See Fig. 9.) Although both the Ar $3p^{-3}3d\,{}^1P$ and $3p^{-3}3d\,{}^3P$ states are populated in atomic Auger decay only via the mixed configuration component $3s^{-1}3p^{-1}$, both the $3p^{-3}3d$ and the $3s^{-1}3p^{-1}$ configurations contribute to ICD: the 3d electron (one of the 3p electrons) in the $3p^{-3}3d$ ($3s^{-1}3p^{-1}$) configuration jumps into the 3p (3s) orbital in the Ar atom by emitting a *virtual* photon, while the other Ar atom which absorbed the virtual photon emits a 3p electron as an ICD electron. The possible final states are combinations of the doubly charged states of $Ar^{2+}(3p^{-2})$ and the singly charged states of $Ar^+(3p^{-1})$.

The possible ICD channels described above are listed in Table 1(a). The two Auger final states $Ar^{2+}(3p^{-3}3d)\,{}^1P$ and ^3P are the initial states of the ICD. The six possible final states are combi-

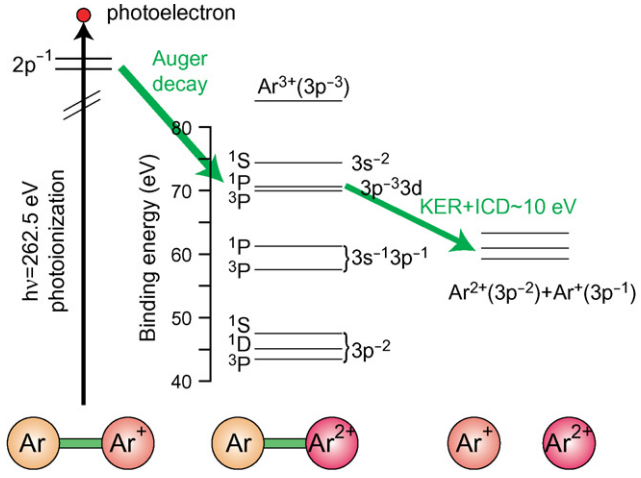

Fig. 9. Schematic energy diagram for the states involved in the interatomic Coulombic decay in Ar_2.

Table 1
State energies and total transition energies for ICD channels in Ar_2 and ArKr after Ar 2p Auger decay

ICD final states		ICD initial states	
$Ar^{2+}(3p^{-2})$	$Ar^{+}(3p^{-1})$	$Ar^{2+}(3p^{-3}3d)\,{}^1P$ 70.65	$Ar^{2+}(3p^{-3}3d)\,{}^3P$ 69.94
(a) $Ar_2 \rightarrow Ar^{2+} + Ar^{+}$			
^1S 47.51	$^2P_{1/2}$ 15.94	A 7.20	(D 6.49)
^1D 45.13	$^2P_{1/2}$ 15.94	B 9.59	(E 8.88)
^3P 43.46	$^2P_{1/2}$ 15.94	(C 11.26)	F 10.55
^1S 47.51	$^2P_{3/2}$ 15.76	A′ 7.38	(D′ 6.67)
^1D 45.13	$^2P_{3/2}$ 15.76	B′ 9.77	(E′ 9.05)
^3P 43.46	$^2P_{3/2}$ 15.76	(C′ 11.44)	F′ 10.72
ICD final states		ICD initial states	
$Ar^{2+}(3p^{-2})$	$Kr^{+}(4p^{-1})$	$Ar^{2+}(3p^{-3}3d)\,{}^1P$ 70.65	$Ar^{2+}(3p^{-3}3d)\,{}^3P$ 69.94
(b) $ArKr \rightarrow Ar^{2+} + Kr^{+}$			
^1S 47.51	$^2P_{1/2}$ 14.67	A 8.48	(D 7.76)
^1D 45.13	$^2P_{1/2}$ 14.67	B 10.86	(E 10.15)
^3P 43.46	$^2P_{1/2}$ 14.67	(C 12.53)	F 11.81
^1S 47.51	$^2P_{3/2}$ 14.0	A′ 9.14	(D′ 8.43)
^1D 45.13	$^2P_{3/2}$ 14.0	B′ 11.53	(E′ 10.81)
^3P 43.46	$^2P_{3/2}$ 14.0	(C′ 13.20)	F′ 12.48

The two Auger final states $Ar^{2+}(3p^{-3}3d)\,{}^1P$ and ${}^3P$ are the initial states of the ICD and are listed with their energies (relative to the neutral ground state) at the top of the right hand columns. The six ICD final states corresponding to combinations between the three doubly charged ionic states $Ar^{2+}(3p^{-2})\,{}^1S$, ${}^1D$ and ${}^3P$ and two singly charged ionic states (a) $Ar^{+}(3p^{-1})\,{}^2P_{1/2}$ and ${}^2P_{3/2}$ or (b) $Kr^{+}(4p^{-1})\,{}^2P_{1/2}$ and ${}^2P_{3/2}$ are listed with their energies in the first two columns (left hand columns). The 12 possible combinations of the initial and final states of the ICD are labelled A–F and A′–F′ in the table. The prime indicates a ${}^2P_{3/2}$ final state for Ar^{+}. The listed energies correspond to the sum of the ICD electron energy and the KER, which can be estimated from the listed energies by $E(Ar^{2+}(3p^{-3}3d)) - E(Ar^{2+}(3p^{-2})) - E(Ar^{+}(3p^{-1}))$ or $E(Kr^{+}(4p^{-1}))$. All energies are given in eV.

nations of the three doubly charged states $Ar^{2+}(3p^{-2})\,{}^1S$, ${}^1D$ and ${}^3P$ and the two single-charged states $Ar^{+}(3p^{-1})\,{}^2P_{1/2}$ and ${}^2P_{3/2}$. The 12 possible combinations of the initial and final states of the ICD are labelled A–F and A′–F′ in the table. The prime indicates a ${}^2P_{3/2}$ final state for Ar^{+}. The listed energies correspond to the sum of the ICD electron energy and the KER, which can be estimated from the listed energies by $E(Ar^{2+}(3p^{-3}3d)) - E(Ar^{2+}(3p^{-2})) - E(Ar^{+}(3p^{-1}))$.

The multiplicity of $Ar^{2+}(3p^{-3}3d)$ in the ICD initial states is either singlet or triplet, and the multiplicity of $Ar^{2+}(3p^{-2})$ in the ICD final states is also either singlet or triplet. Let us assume that LSJ coupling is valid in Ar. Then, in the virtual photon exchange picture, the initial Ar^{2+} singlet (triplet) states decay to Ar^{2+} singlet (triplet) states by emitting a virtual photon, which is absorbed by the other Ar resulting in the emission of the ICD electron: the total spin in Ar^{2+} should be *conserved* in this way. One should however note that ICD can also take place via electron exchange, with a 3p electron in the other Ar atom filling the Ar^{2+} 3p hole, and an Ar^{2+} 3d electron being ejected as the ICD electron. In this case, the spin may appear to *flip* at the Ar^{2+} site. The labels in parentheses in Table 1(a) indicate these spin-flip ICDs.

The ICD channels listed in Table 1(a) are shown in Fig. 7(a) by labelled solid and dotted vertical lines. The heights of the thick vertical lines correspond to the products of the relative populations of the ICD initial states as estimated from the Auger intensities (3:1 for ${}^1P$: ${}^3P$) and the statistical weights of the spin-conserved ICD final states. The spin-flip ICDs are indicated by thin lines, whose heights are scaled relative to the spin-conserved ICDs by the statistical weights of the final states. Lines B and B′ are spin-conserved ICDs and agree well with the maximum of the energy sum distribution. On the other hand, lines C and C′ at high-energy foot of the peak are spin-flip ICDs. Thus our observation indicates that spin-conserved ICDs are stronger than spin-flip ICDs. It is clear that the spin-conserved ICDs F and F′ also contribute to the high-energy tail of the broad energy-sum distribution. The expected energy sums of spin-conserved ICDs are also given in Fig. 5(a) as straight lines of slope −1. These correspond well with the strong island structure. The ICDs A and A′ are outside of the Franck–Condon region as can be seen in Fig. 5(a).

ICD in ArKr after Ar 2p Auger decay can be discussed completely parallel to the ICD in Ar_2 discussed above, by replacing $Ar^{+}(3p^{-1}{}^2P)$ by $Kr^{+}(4p^{-1}{}^2P)$. The possible ICD channels in ArKr after Ar 2p Auger decay are listed in Table 1(b) in the same manner as those in Ar_2 and are shown in Figs. 7(b) and 5(b). The arguments on Ar_2 in Figs. 7(a) and 5(a) are well valid on ArKr in Figs. 7(b) and 5(b). Namely, spin-conserved ICDs lines B, B′, F and F′ form the main broad peak of the energy-sum distribution in Fig. 7(b) and the corresponding four lines well go through the main island structure in Fig. 5(b). The contributions from A and A′ can also be recognizable in Fig. 5(b). On the other hand, it is not possible to clearly identify contributions from the spin-flip ICDs, C, C′, D, D′, E and E′ in Fig. 7(b).

4.2. ICDs after Kr 3d Auger decay

We now consider the ICD in Kr_2 after Kr Auger decay. We consider that ICD occurs after Kr 3d Auger decay. It may be worth noting that, at the present photon energy 262.54 eV, the shake probability at the Kr 3d photoionization, including both shake-up and shake-off, is 0.21–0.25 [42,43]. The atom having 3d and valence holes decays to the triply charged ion [44], emitting a low energy Auger electron. Kinetic energies of such low energy atomic Auger electrons have not been clarified, but very likely close to those of the ICD electrons. The dimer ion that consists of a triply charged Kr^{3+} and a neutral atom Kr or Ar may also dissociate into the ion pair of Kr^{2+}–Kr^{+} or Ar^{+} via charge transfer in the dimer. The non-negligible contribution from these Auger decays from the 3d shake-up and shake-off states, as well as from 3p Auger decay, is not presumed to affect the following discussion significantly.

Fig. 10 shows a schematic energy level diagram relevant to the ICD in Kr_2 after Kr 3d Auger decay. Again the discussion is parallel to the ICD in Ar_2 after Ar 2p Auger decay. In the Auger final states of atomic Kr^{2+}, the two configurations $4s^{-1}4p^{-1}$ and $4p^{-3}4d$ are completely mixed and, as a result, the Auger transition to the state at 62.74 eV, designated as $4p^{-3}4d$, occurs with significant intensity [45].

The possible ICD channels from the Auger final state $Kr^{2+}(4p^{-3}4d)$ discussed above are listed in Table 2(a). The six pos-

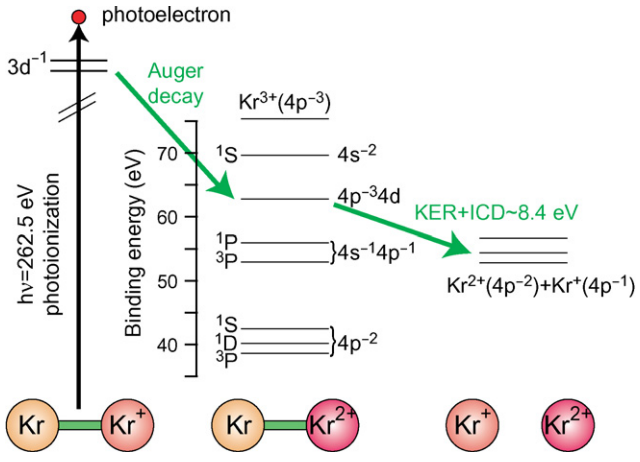

Fig. 10. Schematic energy diagram for the states involved in the interatomic Coulombic decay in Kr_2.

Table 2
State energies and total transition energies for ICDs in Kr_2 and ArKr after Kr 3d Auger decay

ICD final states		ICD initial states	
$Kr^{2+}(4p^{-2})$	$Kr^{+}(4p^{-1})$	$Kr^{2+}(4p^{-3}4d)$ 62.74	$Kr^{2+}(4s^{-2})\ ^1S$ 69.62
(a) $Kr_2 \rightarrow Kr^{2+} + Kr^{+}$			
^1S 42.46	$^2P_{1/2}$ 14.67	A 5.61	D 12.49
^1D 40.18	$^2P_{1/2}$ 14.67	B 7.90	E 14.78
^3P 38.62	$^2P_{1/2}$ 14.67	C 9.45	F 16.33
^1S 42.46	$^2P_{3/2}$ 14.0	A′ 6.28	D′ 13.16
^1D 40.18	$^2P_{3/2}$ 14.0	B′ 8.57	E′ 15.44
^3P 38.62	$^2P_{3/2}$ 14.0	C′ 10.12	F′ 17.0
ICD final states		ICD initial states	
$Kr^{2+}(4p^{-2})$	$Ar^{+}(3p^{-1})$	$Kr^{2+}(4p^{-3}4d)$ 62.74	$Kr^{2+}(4s^{-2})\ ^1S$ 69.62
(b) $ArKr \rightarrow Kr^{2+} + Ar^{+}$			
^1S 42.46	$^2P_{1/2}$ 15.94	A 4.34	D 11.22
^1D 40.18	$^2P_{1/2}$ 15.94	B 6.63	E 13.51
^3P 38.62	$^2P_{1/2}$ 15.94	C 8.18	F 15.06
^1S 42.46	$^2P_{3/2}$ 15.76	A′ 4.52	D′ 11.40
^1D 40.18	$^2P_{3/2}$ 15.76	B′ 6.81	E′ 13.68
^3P 38.62	$^2P_{3/2}$ 15.76	C′ 8.36	F′ 15.24

The two Auger final states $Kr^{2+}4p^{-3}4d$ and $4s^{-2}$ are the initial states of the ICDs and these state energies are given at the top of the first column in the right hand columns. The six ICD final states corresponding to combinations between the three doubly charged ionic states $Kr^{2+}(4p^{-2})\ ^1S$, ^1D and ^3P and the two singly charged ionic states (a) $Kr^{+}(4p^{-1})\ ^2P_{1/2}$ and $^2P_{3/2}$ or (b) $Ar^{+}(3p^{-1})\ ^2P_{1/2}$ and $^2P_{3/2}$ are listed with their energies in the first two columns (left hand columns). The 12 possible combinations of the initial and final states of the ICD are labelled A–C, A′–C′, D–F and D′–F′ in the table. The prime indicates a $^2P_{3/2}$ final state for Kr^+ or Ar^+. The listed energies correspond to the sum of the ICD electron energy and the KER. All energies are given in eV.

sible final states are combinations of the three doubly charged states $Kr^{2+}(4p^{-2})\ ^1S$, ^1D and ^3P and the two singly charged states $Kr^{+}(4p^{-1})\ ^2P_{1/2}$ and $^2P_{3/2}$. The six possible ICD channels are labelled A–C and A′–C′ in the table. The prime indicates a $^2P_{3/2}$ final state for Kr^+. The listed energies correspond to the sum of the ICD electron energy and the KER. These ICD channels are shown in Fig. 8(b) by labelled solid vertical lines. The heights of the lines correspond to the statistical weights. Lines B and B′ well agree with the main peak of the energy-sum distribution in Fig. 8(b), whereas lines C and C′ form the high-energy foot of this peak. In Fig. 6(b), lines B and B′ well go through the strongest island, whereas lines C and C′ go through weak island structure. The ICDs corresponding to lines A and A′ are outside of the Franck–Condon region as can be seen in Fig. 6(b). These observations may imply that the state at 62.74 eV has a singlet $^1P_1$ character that preferentially decays to $Kr^{2+}4p^{-2}\ ^1D_2$. Unambiguous assignment cannot be given to this state because the corresponding state cannot be found in the dicationic energy level diagram compiled by NIST based on optical data [40].

The Auger transition to the state at 69.62 eV, designated as $4s^{-2}\ ^1S$ [40], also occurs with significant intensity [45]. The intensity ratio of the Auger transitions to $4p^{-3}4d$ and to $4s^{-2}\ ^1S$ is roughly 3:2 [45]. The possible ICD channels from the Auger final state $Kr^{2+}(4s^{-2}\ ^1S)$ are listed in Table 2(a). The six possible ICD channels are labelled D–F and D′–F′ in the table. These ICD channels are shown in Fig. 8(b) by labelled dashed vertical lines. The heights of the lines correspond to the statistical weights multiplied by the Auger intensity ratio 2/3 relative to the $4p^{-3}4d$ channel. These lines well correspond to the broad peak structure at ≈16 eV in the energy-sum distribution in Fig. 8(b) and the weak broad island structure in Fig. 6(b). These ICDs are dipole-forbidden and thus the virtual photon exchange picture does not hold. Instead, the ICDs are considered to take place by the overlap of the orbitals. This may well correlate to the fact that there is no strong spin selectivity any more.

ICD in ArKr after Kr 3d Auger decay should be discussed parallel to the ICD in Kr_2 discussed above, by replacing $Kr^{+}(4p^{-1}\ ^2P)$ by $Ar^{+}(3p^{-1}\ ^2P)$. The possible ICD channels are listed in Table 2(b). As can be seen in Fig. 6(a), the ICDs corresponding to lines not only A and A′ but also B and B′, which are dominant ICD channels in Kr_2, are now outside of the Franck–Condon region and only the ICDs to $Kr^{2+}(4p^{-2}\ ^3P) + Ar^{+}(3p^{-1}\ ^2P)$ (Line C and C′), which are minor channels in Kr_2, appear, forming a main peak in Fig. 8(a). This explains the puzzle that the kinetic energies of the ICD electrons after Kr Auger decay are about same for ArKr and Kr_2, in spite of the difference in the ionization energies between Ar and Kr. Recalling that the state at 62.74 eV might have singlet character, the spin-flip ICD channel might become possible due to either electron exchange or spin-orbit interaction that may not be negligible for Kr. A broad feature at an energy-sum of ≈15 eV in Fig. 8(a) and the corresponding weak broad island structure in Fig. 6(a) are well correlated to lines D–F and D′–F′ and thus may be attributed to the dipole-forbidden ICD emission from $Kr^{2+}(4s^{-2}\ ^1S)$–Ar.

We note here that the dominant ICD channel in ArKr after the Ar 2p Auger decay is spin-conserved and dipole-allowed and thus the virtual photon exchange picture holds, whereas the observed ICD channels in ArKr after the Kr 3d Auger decay may be spin-flip or dipole-forbidden and thus the overlap of the orbitals may play a role. This may result in suppression of the ICD rates after Kr 3d Auger decay and explain the different KER distributions observed in Fig. 2(b) and (c).

It is worth noting also that interatomic non-sequential double Auger decay, which directly creates the A^{2+}–B^{+} two-site states, might also be possible, considering the fact that non-sequential double Auger decay was found to be a significant contribution to the Auger intensity in isolated atoms [46–48]. This non-sequential interatomic process emits two electrons with continuous energy distributions and contribute to the formation of the baseline in the spectra of Figs. 3, 7 and 8 and correlation diagram of Figs. 5 and 6. Note also that the non-sequential double Auger emission may come from two different contributions: shake-off, where the electron is shaken off from the neighbor-atom in the dimer, and internal inelastic scattering, where the Auger electron shoots the neighbor-atom and knocks out the electron inelastically. In principle, one can sort out these two mechanisms by observing the angular correlation between the two electrons relative to the dimer axis. The low coincidence counts of the present measurements, however, prevented us from extracting such differential information. Atomic sequential and non-sequential double Auger decay [46–48] in the dimer, which forms A^{3+}–B one-site states that may undergo A^{2+}–B^{+} dissociation via change transfer, might also contribute to the observed coincident signals. Finally, it should also be noticed that the ICD can take place even after atomic non-sequential and sequential double Auger decay [46–48], resulting in A^{3+}–B^{+} ion pair formation.

5. Conclusion

We have identified some ICD processes from the Auger final states of the Ar_2, ArKr and Kr_2 dimers produced by the supersonic expansion of a mixture of Ar and Kr gases, by simultaneously determining the kinetic energy of the ICD electron and the KER of the two ion pairs A^{2+}–B^{+}, using momentum-resolved electron–ion–ion coincidence spectroscopy. The neutral atom B, stuck to the dication A^{2+} produced via the atomic Auger decay of atom A, can be regarded as the environment. This environment opens ICD channels that are energetically forbidden for an isolated dication A^{2+}. We find that spin-conserved ICD, which can be viewed as energy

transfer to the environment (atom B) via virtual photon exchange, is significantly stronger than spin-flip ICD and that the spin-flip ICD can occur when the virtual photon exchange channel is energetically forbidden. Dipole-forbidden ICD can also be seen. We note that ICDs following atomic Auger decay are very general decay channels which lead to the emission of low-energy electrons following inner-shell ionization. These processes are thus relevant to numerous physical, chemical, and biological phenomena involving inner-shell vacancies in clusters and other forms of spatially extended atomic and molecular matter, including biomolecules in living cells.

Acknowledgements

The experiments were performed at SPring-8 with the approval of JASRI (2007A1394-NSb-np and 2007A1602-NSb-np). The authors are grateful to S. Stoychev, A. Kuleff, V. Averbukh and L.S. Cederbaum for discussion on theoretical aspects. The work was supported by Grants-in-Aid for Scientific Research from the Japan Society for Promotion of Science (JSPS), by the Budget for "Promotion of X-ray Free Electron Laser Research" from Ministry of Education, Culture, Sports, Science and Technology (MEXT), and by BMBF and DFG. XJL acknowledges JSPS for financial support. KK acknowledges financial support by DESY and the HGF Initiative and Networking Fund.

References

[1] M. Thompson, M.D. Baker, A. Christie, J.F. Tyson, Auger Electron Spectroscopy, Wiley, New York, 1985.
[2] F. Tarantelli, L.S. Cederbaum, Phys. Rev. Lett. 71 (1993) 649.
[3] L.S. Cederbaum, J. Zobeley, F. Tarantelli, Phys. Rev. Lett. 79 (1997) 4778.
[4] S. Marburger, O. Kugeler, U. Hergenhahn, T. Möller, Phys. Rev. Lett. 90 (2003) 203401.
[5] T. Jahnke, A. Czasch, M.S. Schöffler, S. Schössler, A. Knapp, M. Käsz, J. Titze, C. Wimmer, K. Kreidi, R.E. Grisenti, A. Staudte, O. Jagutzki, U. Hergenhahn, H. Schmidt-Böcking, R. Dörner, Phys. Rev. Lett. 93 (2004) 163401.
[6] T. Jahnke, Th. Weber, T. Osipov, A.L. Landers, O. Jagutzki, L.Ph.H. Schmidt, C.L. Cocke, M.H. Prior, H. Schmidt-Böcking, R. Dörner, J. Electr. Spectrosc. Relat. Phenom. 141 (2004) 229.
[7] J. Ullrich, R. Moshammer, A. Dorn, R. Dörner, L.Ph.H. Schmidt, H. Schmidt-Böcking, Rep. Prog. Phys. 66 (2003) 1463.
[8] R. Santra, J. Zobeley, L.S. Cederbaum, N. Moiseyev, Phys. Rev. Lett. 85 (2000) 4490.
[9] T. Jahnke, A. Czasch, M. Schöffler, S. Schössler, M. Käsz, J. Titze, K. Kreidi, R.E. Grisenti, A. Staudte, O. Jagutzki, L.Ph. Schmidt, Th. Weber, H. Schmidt-Böcking, K. Ueda, R. Dörner, Phys. Rev. Lett. 99 (2007) 153401.
[10] V. Averbukh, I.B. Müller, L.S. Cederbaum, Phys. Rev. Lett. 93 (2004) 263002.
[11] V. Averbukh, L.S. Cederbaum, Phys. Rev. Lett. 96 (2006) 053401.
[12] R. Santra, J. Zobeley, L.S. Cederbaum, Phys. Rev. B 64 (2001) 245104.
[13] G. Öhrwall, M. Tchaplyguine, M. Lundwall, R. Feifel, H. Bergersen, T. Rander, A. Lindblad, J. Schulz, S. Peredkov, S. Barth, S. Marburger, U. Hergenhahn, S. Svensson, O. Björneholm, Phys. Rev. Lett. 93 (2004) 173401.
[14] S. Svensson, J. Phys. B: At. Mol. Opt. Phys. 38 (2005) S821.
[15] S. Barth, S. Joshi, S. Marburger, V. Ulrich, A. Lindblad, G. Öhrwall, O. Björneholm, U. Hergenhahn, J. Chem. Phys. 122 (2005) 241102.
[16] T. Aoto, K. Ito, Y. Hikosaka, E. Shigemasa, F. Penent, P. Lablanquie, Phys. Rev. Lett. 97 (2006) 243401.
[17] P. Lablanquie, T. Aoto, Y. Hikosaka, Y. Morioka, F. Penent, K. Ito, J. Chem. Phys. 127 (2007) 154323.
[18] R. Santra, L.S. Cederbaum, Phys. Rev. Lett. 90 (2003) 153401; R. Santra, L.S. Cederbaum, Phys. Rev. Lett. 94 (2005) 199901(E).
[19] Y. Morishita, X.-J. Liu, N. Saito, T. Lischke, M. Kato, G. Prümper, M. Oura, H. Yamaoka, Y. Tamenori, I.H. Suzuki, K. Ueda, Phys. Rev. Lett. 96 (2006) 243402.
[20] S.D. Stoychev, A.I. Kuleff, F. Tarantelli, L.S. Cederbaum, J. Chem. Phys. 128 (2008) 014307.
[21] Y. Morishita, N. Saito, I.H. Suzuki, H. Fukuzawa, X.-J. Liu, K. Sakai, G. Prümper, K. Ueda, H. Iwayama, K. Nagaya, M. Yao, K. Kreidi, M. Schöffler, T. Jahnke, S. Schössler, R. Dörner, Th. Weber, J. Harries, Y. Tamenori, J. Phys. B: At. Mol. Opt. Phys. 41 (2008) 025101.
[22] H. Ohashi, E. Ishiguro, Y. Tamenori, H. Kishimoto, M. Tanaka, M. Irie, T. Tanaka, T. Ishikawa, Nucl. Instrum. Methods A 467–468 (2001) 529.
[23] H. Ohashi, E. Ishiguro, Y. Tamenori, H. Okumura, A. Hiraya, H. Yoshida, Y. Senba, K. Okada, N. Saito, I.H. Suzuki, K. Ueda, T. Ibuki, S. Nagaoka, I. Koyano, T. Ishikawa, A 467–468 (2001) 533.
[24] K. Ueda, J. Phys. B: At. Mol. Opt. Phys. 36 (2003) R1.
[25] G.C. King, M. Tronc, F.H. Read, R.C. Bradford, J. Phys. B: At. Mol. Opt. Phys. 10 (1977) 2479.
[26] Y. Muramatsu, K. Ueda, N. Saito, H. Chiba, M. Lavollée, A. Czasch, Th. Weber, O. Jagutzki, H. Schmidt-Böcking, R. Moshammer, K. Kubozuka, I. Koyano, Phys. Rev. Lett. 88 (2002) 133002.
[27] A. De Fanis, N. Saito, A.A. Pavlychev, D.Yu. Ladonin, M. Machida, K. Kubozuka, I. Koyano, K. Okada, K. Ikejiri, A. Cassimi, A. Czasch, R. Dörner, H. Chiba, Y. Sato, K. Ueda, Phys. Rev. Lett. 89 (2002) 023006.
[28] K. Ueda, J.H.D. Eland, J. Phys. B: At. Mol. Opt. Phys. 38 (2005) S839.
[29] N. Saito, A. De Fanis, I. Koyano, K. Ueda, J. Electron Spectrosc. Relat. Phenom. 144–147 (2005) 103.
[30] Y. Morishita, M. Kato, G. Prümper, X.-J. Liu, T. Lischke, K. Ueda, Y. Tamenori, M. Oura, H. Yamaoka, I.H. Suzuki, N. Saito, Radiat. Phys. Chem. 75 (2006) 1977.
[31] K. Ueda, X.-J. Liu, G. Prümper, H. Fukuzawa, Y. Morishita, N. Saito, J. Electr. Spectrosc. Relat. Phenom. 155 (2007) 113.
[32] N. Saito, X.-J. Liu, Y. Morishita, I.H. Suzuki, K. Ueda, J. Electr. Spectrosc. Relat. Phenom. 156–158 (2007) 68.
[33] O. Jagutzki, A. Cerezo, A. Czasch, R. Dörner, M. Hattaß, M. Huang, V. Mergel, U. Spillmann, K. Ullmann-Pfleger, Th. Weber, H. Schmidt-Böcking, G.D.W. Smith, IEEE Transact. Nucl. Science 49 (2002) 2477.
[34] Y. Morishita, Y. Tamenori, M. Machida, M. Oura, H. Yamaoka, H. Ohashi, M. Suzuki, H. Toyokawa, A. De Fanis, M. Nagoshi, I. Koyano, K. Fujiwara, H. Chiba, G. Prümper, K. Ueda, I.H. Suzuki, N. Saito, J. Electron Spectrosc. Relat. Phenom. 144–147 (2005) 255.
[35] J.F. Ogilvie, F.Y.H. Wang, J. Mol. Struct. 273 (1992) 277.
[36] J.F. Ogilvie, F.Y.H. Wang, J. Mol. Struct. 291 (1992) 313.
[37] J. Zobeley, R. Santra, L.S. Cederbaum, J. Chem. Phys. 115 (2001) 5076.
[38] S. Svenson, N. Mårtensson, E. Basilier, P.Å. Malmquist, U. Gellius, K. Siegbahn, Phys. Scr. 14 (1976) 141.
[39] D.W. Lindle, P.A. Heimann, T.A. Ferrett, P.H. Kobrin, C.M. Truesdale, U. Becker, H.G. Kerkhoff, D.A. Shirley, Phys. Rev. A 33 (1986) 319.
[40] http://physics.nist.gov/PhysRefData/ASD/levels_form.html.
[41] H. Pulkkinen, S. Aksela, O.-P. Sairanen, A. Hiltunen, H. Aksela, J. Phys. B: At. Mol. Phys. 29 (1966) 3033.
[42] L. Partanen, M. Huttula, H. Aksela, S. Aksela, J. Phys. B: At. Mol. Opt. Phys. 40 (2007) 3795.
[43] N. Saito, I.H. Suzuki, Phys. Script. 49 (1994) 80.
[44] Y. Tamenori, K. Okada, S. Tanimoto, T. Ibuki, S. Nagaoka, A. Fujii, Y. Haga, I.H. Suzuki, J. Phys. B: At. Mol. Opt. Phys. 37 (2004) 117.
[45] J. Jauhiainen, H. Aksela, S. Aksela, A. Kivimäki, O.-P. Sairanen, E. Nõmmiste, J. Végh, J. Phys. B: At. Mol. Phys. 28 (1995) 3831.
[46] J. Viefhaus, S. Cvejanovi, B. Langer, T. Lischke, G. Prümper, D. Rolles, A.V. Golovin, A.N. Grum-Grzhimailo, N.M. Kabachnik, U. Becker, Phys Rev. Lett. 92 (2004) 083001.
[47] J. Viefhaus, M. Braune, S. Korica, A. Reinköster, D. Rolles, U. Becker, J. Phys. B: At. Mol. Opt. Phys. 38 (2005) 3885.
[48] P. Lablanquie, L. Andric, J. Palaudoux, U. Becker, M. Braune, J. Viefhaus, J.H.D. Eland, F. Penent, J. Electr. Spectrosc. Relat. Phenom. 156 (2007) 51.